Experiments performed with bubbly flow in vertical pipes at different flow conditions covering the transition region: simulation by coupling Eulerian, Lagrangian and 3D random walks models

JOSÉ L. MUÑOZ-COBO[1][*]
SERGIO CHIVA[2]
MOHAMED ALI ABD EL AZIZ ESSA[1]
SANTOS MENDES[3]

[1] Universidad Politécnica de Valencia, Instituto Ingeniería Energética, Spain

[2] Universitat Jaume I de Castelló, Departamento de Ingeniería Mecánica y Construcción, Spain

[3] Facultad de Ingeniería Mecánica y Eléctrica, Universidad Autónoma de Nuevo León, México

Abstract Two phase flow experiments with different superficial velocities of gas and water were performed in a vertical upward isothermal co-current air-water flow column with conditions ranging from bubbly flow, with very low void fraction, to transition flow with some cap and slug bubbles and void fractions around 25%. The superficial velocities of the liquid and the gas phases were varied from 0.5 to 3 m/s and from 0 to 0.6 m/s, respectively. Also to check the effect of changing the surface tension on the previous experiments small amounts of 1-butanol were added to the water. These amounts range from 9 to 75 ppm and change the surface tension. This study is interesting because in real cases the surface tension of the water diminishes with temperature, and with this kind of experiments we can study indirectly the effect of changing the temperature on the void fraction distribution. The following axial and radial distributions were measured in all these experiments: void fraction, interfacial area concentration, interfa-

[*]Corresoponding author. E-mail address: jlcobos@iqn.upv.es

cial velocity, Sauter mean diameter and turbulence intensity. The range of values of the gas superficial velocities in these experiments covered the range from bubbly flow to the transition to cap/slug flow. Also with transition flow conditions we distinguish two groups of bubbles in the experiments, the small spherical bubbles and the cap/slug bubbles. Special interest was devoted to the transition region from bubbly to cap/slug flow; the goal was to understand the physical phenomena that take place during this transition A set of numerical simulations of some of these experiments for bubbly flow conditions has been performed by coupling a Lagrangian code, that tracks the three dimensional motion of the individual bubbles in cylindrical coordinates inside the field of the carrier liquid, to an Eulerian model that computes the magnitudes of continuous phase and to a 3D random walk model that takes on account the fluctuation in the velocity field of the carrier fluid that are seen by the bubbles due to turbulence fluctuations. Also we have included in the model the deformation that suffers the bubble when it touches the wall and it is compressed by the forces that pushes it toward the wall, provoking that the bubble rebound like a ball.

Nomenclature

$\underline{a}(\underline{X}(t), t)$	–	drift term of the stochastic differential equation
$\underline{b}(t)$	–	difussion coefficient of the stochastic differential equation
C_D	–	drag coefficient
C_v	–	coefficientt of virtual mass force
D	–	tube diameter, and conductivity probe diameter
d_b	–	bubble diameter
d_{needle}	–	tip diameter
Eo	–	Eötvos adimensional number
$\hat{e}$	–	unit vector
f_i	–	interfacial force per unit volume
F	–	force
g	–	gravitational acceleration
j	–	superficial velocity
k	–	turbulent kinetic energy
M_g	–	molecular weight of the gas
$N(0,1)$	–	normal distribution of zero mean and unity variance
N_μ	–	viscosity adimensional number
$\vec{n}_{I,j}$	–	unit vector normal to the j-th interface
p	–	pressure
r	–	radial coordinate
R	–	tube radius
R_b	–	bubble radius
R_g	–	universal constant of the gases
Re	–	Reynolds number

S	–	area
ΔS_{0k}	–	distance from the front tip to the k-th rear tip
T	–	temperature
T_i	–	($i = 1, 2, 3, 4$) tips of the conductivity probe sensors
t	–	time
u	–	velocity
u^*	–	friction velocity
u'	–	fluctuating component of the velocity
$\vec{u}_{m,0k}$	–	measured velocity in the direction of the unit vector $\hat{e}_{0k}$
V	–	volume
W	–	work
$W(t)$	–	Wiener process at time t
y	–	distance from the bubble centre to the wall
z	–	axial coordinate

Greek symbols

α	–	void fraction
α_l	–	liquid fraction
Δ	–	time integration step
κ	–	Von-Karman constant
θ	–	azimuthal coordinate
μ	–	viscosity
ρ	–	density
ν	–	kinematic viscosity
σ	–	surface tension
σ_r	–	normal stress in the radial direction
ξ	–	Gaussian random number with $N(0,1)$ distribution
τ_w	–	shear stress of the fluid at the wall
τ_L	–	Lagrangian time scale
$\vec{\omega}$	–	vorticity of the liquid velocity field

Subscripts

b	–	bubble
D	–	drag
Def	–	deformation
d	–	distorted
f	–	continuous fluid phase (liquid)
g	–	gas
l	–	liquid
r	–	component in the radial direction
WL	–	wall lubrication
L	–	lift
z	–	component in the axial direction
w	–	wall
θ	–	component in the azimuthal direction
t	–	turbulent

1 Introduction

The recent interest in two phase flow arises from its extreme importance in several industrial applications, such as chemical reactor, nuclear reactor cooling, oil transportation and many others [1]. The dynamics of two phases consists in a set of phenomena that must be considered simultaneously. It involves all the difficulties associated to describing single phase flows plus a set of two-phase aspects such as interfacial boundary locations, inter-phase momentum exchange, heat and mass transfer between phases, turbulence induced by the gas phase on the liquid phase. In order to have good predictions of the bubble's motion in two phase problems there is required a correct description of the interactions that take place between the dispersed and continuous phases in both the near-wall and the unbounded flow regions [2]. Many experimental measurements and numerical simulations have been performed in recent years to better understand the bubble behaviour in vertical gas-liquid flows. Important contributions in this area have been performed by different research groups [2–6].

A better knowledge of the different forces that act on the bubbles moving in a continuous turbulent random fluid field is of importance for a complete description of the bubble's motion and to obtain the radial and axial distributions of void fraction, interfacial area concentration, and the gas phase velocity inside the reactor channels [7]. Normally for bubbly flow the lift force produces a radial force that pushes the small size bubbles toward the wall. Near the wall the lubrication and the deformation forces tend to separate the bubbles from the wall, producing a peak in the void fraction near the wall that is called the wall peak. But if one considers these forces only, the height of the wall peak that results is normally too high as compared with the experimental data. For this reason, it is necessary to have a model that diffuses the bubbles away from the wall peak. This effect is accomplished by adding a 3D random walk model that takes on account the fluctuation in velocity of the continuous phase (liquid), produced by turbulence. Here it is important to consider the turbulence due to the liquid and the turbulence induced by the bubbles.

Experiments specifically designed to understand the forces that act on the bubbles are a tool necessary to validate the models that predict the forces acting on the bubbles and to develop new ones. With this goal in mind, an upward isothermal cocurrent air-water flow in a vertical pipe (52 mm inner diameter) has been experimentally investigated. Local measurements of void fraction, interfacial area concentration (IAC), interfacial

velocity and the Sauter mean diameter were performed using a four sensor conductivity probe. Liquid velocity and turbulence intensity were also measured using the laser Doppler anemometry (LDA). Different air-water flow configurations were investigated for liquid superficial velocities ranging from 0.491 to 3 m/s and a void fraction up to 25%. For each two-phase flow configuration 15 radial position and three axial locations were measured by the conductivity probe methodology, and several radial profiles were also measured with LDA at different axial positions.

The reason to perform detailed experiments near the transition region with void fractions around 25% is that the bubbles becomes larger due to the coalescence produced by the interaction between neighboring bubbles that is a more probable event when the void fraction increases. In this case for these larger bubbles the lift force reverses its sign and pushes these larger bubbles toward the centre of the pipe, producing the so called core peak distribution because the void fraction is larger at the central region than near the walls.

An important issue is to understand how the flow regime map, changes the size of bubbles and the bubble distribution when temperature rises as happens in nuclear energy reactors, or any other energy system. Normally these changes are produced mainly by the reduction of the surface tension with temperature. In order to understand the physics behind these changes we have performed a set of experiments where we have reduced the surface tension by adding small quantities of 1-butanol. The surface tension has been reduced in these experiments between 4 and 8% depending of the amount of 1-butanol added. Interesting modifications of the void fraction distribution and the flow map have found in these experiments and will be explained in Section 4 of this paper.

A set of numerical simulations of these experiments for bubbly flow conditions were performed by coupling a Lagrangian code, that tracks the 3D motion of the individual bubbles under the buoyancy, lift, drag and near wall forces to an Eulerian model that computes the continuous phase. Also, we incorporate a 3D Langevin-type model to account for the random motion of the individual bubbles in the turbulent velocity field of the carrier liquid. This type of models denoted as continuous random walk models are used to predict the turbulent diffusion of the bubbles in the fluctuating velocity field of the carrier fluid [8–10]. Also we have considered the deformations that suffer the bubbles when they touch the walls of the pipe and are compressed until they rebound.

The velocity and turbulence fields of the liquid phase were computed by solving the time dependent mass, energy, and momentum conservation equations in its Reynolds averaged Navier-Stokes (RANS)equations form . The turbulent kinetic energy k, and the dissipation rate ε transport equations were simultaneously solved by using the k-ϵ model in a (r,z) grid using the finite volume method using the SIMPLER algorithm [34]. Both Lagrangian and Eulerian calculations were performed in parallel taking into account the turbulence induced by the bubbles on the liquid phase. Also the Lagrangian and 3D random walk models were coupled to a 3D Eulerian solver in order to study the differences produced by considering the simplifying assumption of considering an axisymmetric Eulerian model for the continuous phase.

The paper has been organized as follows: Section 2.1 is devoted to explain the Lagrangian model and the different forces acting on the bubbles including the deformation one near the walls. Section 2.2 explains the 3D continuous random walk model, used to compute the instantaneous fluid velocities that are seen by the bubbles in a Lagrangian frame and the importance of the turbulence induced by the bubbles in this model. Also we explain the connection with the Eulerian computational fluid dynamics (CFD) model for the continuous phase in 2D and 3D dimensions. Section 2.3 explains the governing equations for the continuous Eulerian CFD model in cylindrical geometry. Section 3 is devoted to explain the details of the experimental facility, instrumentation used in experiments, signal processing, methods used to obtain the physical magnitudes from the signals and the set of experiments performed to measure the void fraction, velocity distribution of both phases and other typical magnitudes of the biphasic flow. Section 4 is devoted to explain the experiments where we have diminished the surface tension of water by adding small quantities of 1-butanol. Finally Section 5 presents the computational results and the comparison with some experimental results and Section 6 the conclusions.

2 Lagrangian, Eulerian, and 3D random walk models

2.1 Lagrangian model for the bubbles

In cylindrical coordinates (r, θ, z) the motion equations for the bubbles are given by [11]:

$$\left(\rho_g + C_v \rho_l\right) V_b \left(\ddot{r} - r\dot{\theta}^2\right)_b = \sum_i F_{i,r} \,, \tag{1}$$

$$\left(\rho_g + C_v \rho_l\right) V_b \left(r\ddot{\theta} + 2\dot{r}\dot{\theta}\right)_b = \sum_i F_{i,\theta} \,, \tag{2}$$

$$\left(\rho_g + C_v \rho_l\right) V_b \ddot{z}_b = \sum_i F_{i,z} \,, \tag{3}$$

where $F_{i,r}$, $F_{i,\theta}$, $F_{i,z}$ are the radial, azimuthal and axial components of the i-th force acting on the bubble, and the dot on the coordinate components means derivation with respect the time. The components of the velocity of the bubble in cylindrical coordinates are denoted by $(u_r, u_\theta, u_z)_b = (\dot{r}, r\dot{\theta}, \dot{z})_b$. C_v is the coefficient of the virtual mass force which is assumed equal to 0.5, V_b is the volume of the bubble.

The main forces that act on the bubble are the buoyancy force, drag force, lift force, wall-lubrication force and the deformation force. The buoyancy force acting on the bubble is directed in the positive axial direction and its components are given by:

$$F_{br} = 0, \quad F_{b\theta} = 0, \quad F_{bz} = V_b \left(\rho_l - \rho_g\right) g \,, \tag{4}$$

where ρ_l and ρ_g are liquid and gas density, and g is the gravitational acceleration. The drag force $(\vec{F}_D)$ acting on the bubble depends on the relative velocity between the bubble and the continuous phase (liquid), and is given by the following expression:

$$\vec{F}_D = -\frac{3}{8} C_D \frac{1}{R_b} \rho_l V_b \left|\vec{u}_{rel}\right| \vec{u}_{rel} \,, \tag{5}$$

where $\vec{u}_{rel} = \vec{u}_b - \vec{u}_l$ is the relative velocity that acts on the bubble at a given position in the liquid velocity field and R_b is the bubble radius, we note that the liquid velocity in expression (5) is computed as the average velocity of the liquid computed by the Eulerian code plus the fluctuating velocity due to turbulent eddies computed by the 3D random walk model,

as we will explain later. For the drag coefficient (C_D) we have used the expression given by [12]:

$$C_D = \max\left[\min\left\{\frac{16}{\mathrm{Re}_b}\left(1 + 0.15\,\mathrm{Re}_b^{0.687}\right), \frac{48}{\mathrm{Re}_b}\right\}, \frac{8}{3}\frac{\mathrm{Eo}_b}{\mathrm{Eo}_b + 3}\right], \quad (6)$$

where Re_b and Eo_b are the bubble Reynolds and the bubble Eötvos numbers, respectively.

The experiments that have been performed in vertical pipes with bubbly flow showed that the relatively small bubbles tend to migrate toward the wall while the large bubbles tend to migrate toward the centre. This radial motion is attributed to the so called lift force, and is due to the motion of a particle in a fluid field with a velocity gradient in the lateral direction to the main axial motion; this gradient causes a shear field and the motion of the particle in this shear field produce a lateral force. The first analytical expression for the lift force was deduced by Auton [13] for the case of a spherical particle moving in a velocity gradient of an inviscid fluid. Then this expression was extended by Tomiyama *et al.* who considered the interaction between the bubble and the shear field of the fluid [12], and also considered the deformation of the bubble. This lift force acting on the bubbles is given according to Tomiyama [14] by the following expression:

$$\vec{F}_L = -C_T\,V_b\,\rho_l\,(\vec{u}_b - \vec{u}_l) \times \vec{\omega}, \quad (7)$$

where $\vec{\omega}$ is the vorticity of the liquid velocity field, $\vec{\omega} = \vec{\nabla} \times \vec{u}_l$, and C_T is the Tomiyama lift force coefficient that takes into account the interaction between the distorted bubble and the shear field of the liquid phase and is given by:

$$C_T = \begin{cases} \min\left[0.288\ \tanh\left(0.121\mathrm{Re}_b\right), f(\mathrm{Eo}_d)\right] & \text{for}\quad \mathrm{Eo}_d < 4, \\ f(\mathrm{Eo}_d) & \text{for}\quad 4 < \mathrm{Eo}_d < 10, \\ -0.27 & \text{for}\quad \mathrm{Eo}_d > 10, \end{cases} \quad (8)$$

where Eo_d denotes an Eötvos modified number, given in terms of the maximum horizontal dimension of the bubble d_{hb} by:

$$\mathrm{Eo}_d = \frac{g(\rho_l - \rho_g)d_{hb}^2}{\sigma},$$

with

$$d_{hb} = d_b\sqrt[3]{1 + 0.163\mathrm{Eo}^{0.757}},$$

$$(9)$$

and $f(\mathrm{Eo}_d)$ is the function defined by Tomiyama [12]:

$$f(\mathrm{Eo}_d) = 0.00105\,\mathrm{Eo}_d^3 - 0.0159\,\mathrm{Eo}_d^2 - 0.0204\,\mathrm{Eo}_d + 0.474 \ . \qquad (10)$$

We note that the coefficient C_T, defined by Tomiyama in Eq. (8), becomes negative when the bubble diameter becomes bigger than 5.8 mm. This means that for big bubbles the lift force has opposite direction than for small bubbles.

The vorticity in cylindrical coordinates is computed by means of the expression:

$$\vec{\omega} = \frac{1}{r} \begin{vmatrix} \hat{e}_r & r\hat{e}_\theta & \hat{e}_z \\ \frac{\partial}{\partial r} & \frac{\partial}{\partial \theta} & \frac{\partial}{\partial z} \\ 0 & 0 & u_{lz}(r) \end{vmatrix} = -\frac{\partial u_{lz}(r)}{\partial r}\hat{e}_\theta \ . \qquad (11)$$

Because the CFD simulations shows that the velocity profile can be approximated by a logarithmic one, we have assumed that the average fluid velocity profile in the z-direction that is being used to compute the vorticity depends on the radial coordinate in the developed flow region and is given by:

$$\begin{aligned} u_{lz}(r) &= \left\{ \frac{1}{\kappa}\ln\left(\frac{(R-r)u^*}{\nu}\right) + B \right\} u^* && \text{for} \quad 0 < r < R - \frac{5\nu}{u^*} \ , \\ u_{lz}(r) &= \left\{ \frac{(R-r)u^*}{\nu} \right\} u^* && \text{for} \quad R - \frac{5\nu}{u^*} < r < R \ , \end{aligned} \qquad (12)$$

where $u^* = \sqrt{\tau_w/\rho_l}$, being τ_w the shear stress at the pipe wall, and the constants B and κ are: $B = 5$, and $\kappa = 0.41$ is the von Karman constant. Being R the pipe radius, and ν is the kinematic viscosity.

Therefore on account of Eqs. (7), (11) and (12) the expression for the lift force is given in cylindrical coordinates:

$$\vec{F}_L \approx -C_T\,V_b\,\rho_l(u_{bz} - u_{lz})\omega_\theta\hat{e}_r \ , \qquad (13)$$

where ω_θ represents azimuthal vorticity component. We have neglected the axial component of the lift force because is completely negligible in comparison with the axial buoyancy force.

On account of Eq. (11) for the vorticity and Eqs. (12) and (13), the lift

force inside a pipe can be computed by means of the following expression:

$$
\vec{F}_L = \begin{cases} C_T\, V_b\, \rho_l\, (u_{bz} - u_{lz}) \left[\dfrac{u^*}{\kappa\,(R-r)} \right]\, \hat{e}_r\ , & 0 < r < R - \dfrac{5\nu}{u^*}\ , \\[3mm] C_T\, V_b\, \rho_l\, (u_{bz} - u_{lz}) \left[\dfrac{(u^*)^2}{\nu} \right]\, \hat{e}_r\ , & R - \dfrac{5\nu}{u^*} < r < R\ . \end{cases} \tag{14}
$$

The next force considered in the model is the bubble deformation force. According to Zaruba *et al.* [7], we need to take into account this force to prevent the displacement of the bubble centre of mass to be unrealistically close to the wall. To compute this force we have assumed a bubble that when approaching and touching the walls deforms and adopts an oblate elipsoidal shape as displayed in Fig. 1. We have assumed that the deformation of the bubble conserves the volume.
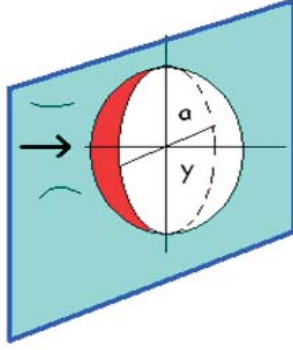
Figure 1. Bubble deforming while its gravity centre approach to the wall.

The work that is needed to deform the bubble from the spherical form to the ellipsoidal oblate one with distance y from the wall to the bubble centre is:

$$
W(y) = \sigma\, \Delta S = \sigma \big[S(y) - S(y = R_b) \big]\ , \tag{15}
$$

where σ is the surface tension, and $S(y)$ is the surface area of the oblate ellipsoid displayed in Fig. 1 with the two semi axes parallel to the wall equal to a, and the semiaxis orthogonal to the wall equal to y. The volume conservation imposes the restriction:

$$
\frac{4}{3}\pi\, R_b^3 = \frac{4}{3}\pi\, a^2 y\ . \tag{16}
$$

Therefore the corresponding force acting on a single bubble with $y = R - r$ is given on account that $\hat{e}_y = -\hat{e}_r$ by:

$$\vec{F}_{Def} = -\frac{\partial W(y)}{\partial y}\hat{e}_y = 2\pi R_b \sigma \left(\frac{R_b}{y}\right)^2 f_D \left(\frac{R_b}{y}\right) \hat{e}_r , \qquad (17)$$

where we have defined the following function that depends only on R_b/y,

$$f_D \left(\frac{R_b}{y}\right) = -1 + \frac{1}{2}\frac{\sinh^{-1}\mu'}{\mu'}\left(\frac{R_b}{y}\right)^{-3/2} +$$
$$+\frac{3}{2}\left(\frac{R_b}{y}\right)^{3/2}\frac{1}{\mu'^{5/2}}\left(\sinh^{-1}\mu' - \frac{\mu'}{(1+\mu'^2)^{1/2}}\right) . \qquad (18)$$

This deformation force ($\vec{F}_{Def}$) is directed toward the centre of the tube and after the bubble compression can provoke the bouncing of the bubble as showed in Zaruba *et al.* experiments [7]. We also note that $\mu'=(R_b^3/y^3-1)^{1/2}$.

The last force considered in the Lagrangian model is the wall lubrication force. This force is originated as a consequence of the drainage of liquid around a bubble that is moving in the vicinity of the pipe wall. The no-slip condition at the wall should slow the drainage rate between the bubble and the wall, at the bubble-wall side, while the drainage of liquid is increased on the opposite side of the bubble. Therefore we have a asymmetrical drainage of liquid for a bubble moving close to the wall. As a consequence the bubble suffers a hydrodynamic force known as wall lubrication force. The expression for this force was first deduced by Antal *et al.* [15], and then improved by Tomiyama *et al.* [5]:

$$\vec{F}_{WL} = -C_{WL} V_b \rho_l |u_{bz} - u_{lz}|^2 f_{wL}(r) \hat{e}_r . \qquad (19)$$

The coefficient of Tomiyama and Hosokawa [14] for the wall lubrication force is given in terms of the bubble Reynolds number and the Eotvos bubble number, which is the ratio of the buoyancy to surface tension forces acting on the bubble:

$$C_{WL} = \max\left\{\frac{7}{\mathrm{Re}_b^{1.9}}, 0.0217\,\mathrm{Eo}_b\right\} , \qquad (20)$$

and the function $f_{wL}(r)$ that defines the wall lubrication forces near the wall is:

$$f_{wL}(r) = d_b \left\{\frac{1}{(R-r)^2} - \frac{1}{(R+r)^2}\right\} , \qquad (21)$$

being R the tube radius and d_b the sphere equivalent diameter of the bubble.

2.2   The continuous 3D random walk model

An approach commonly used to simplify the calculations is to predict the time-averaged velocity of the carrier liquid and the turbulence properties of the continuous phase by solving the random averaged Navier-Stokes equations, and then to use the turbulence parameters values k-ε obtained at the different points of the space $\vec{r}$ to build a statistical model that gives the instantaneous fluid fluctuation velocities that are seen by the bubbles in the Lagrangian frame. If $\vec{r}_b(t)$ denotes the trajectory of the bubble then the turbulence and the dissipation rate seen by the bubbles must be computed at the trajectory points were the bubbles are located, that obviously change with time. Additionally, we must take also into account the turbulence induced by the bubbles themselves that depends of its position inside the pipe and the bubble distribution.

Therefore, the average velocity of the carrier liquid is computed by solving the random averaged Navier-Stokes equations with the k-ε model or any other turbulence model in cylindrical coordinates. However the liquid velocity $\vec{u}_l = \vec{\bar{u}}_l + \vec{u}_l'$ that appears in Eqs. (5), (7), (13), and (22) is composed of an average part $\vec{\bar{u}}_l$ that is computed solving the RANS equations and a fluctuating part $\vec{u}_l'$ due to the eddies, that is obtained by means of a continuous random walk model in 3D, with homogeneous isotropic turbulence, that in the region where the flow is completely developed we have assumed obeys the following stochastic differential equation (SDE) [16–18]:

$$d\vec{u}_l' = -\frac{\vec{u}_l'}{\tau_L(r,z)}dt + \left(\frac{2}{\tau_L(r,z)}\right)^{1/2}\sqrt{\frac{2k(r,z)}{3}}\,d\vec{W}\,, \qquad (22)$$

where $k(r,z)$ denotes the turbulent kinetic energy per unit mass at point (r,z), and we have assumed, to simplify the calculations, that there is no azimuthal dependency by the symmetry of the problem, $\tau_L(r,z)$ is the characteristic time of the Lagrangian time scale correlation [19], that depends of the position, and because of the symmetry of the problem we also assume does not depend of the azimuthal coordinate. We note that because Eq. (22) is in cylindrical coordinates we must include the variations of the unitary vectors of curvilinear coordinates along the fluid particle trajectories. Finally the vector $d\vec{W}$ denotes the infinitesimal increment of a vector valued Wiener process with the well known mean and covariance properties [16]:

$$\langle d\vec{W}\rangle = 0 \quad \text{and} \quad \langle dW_i dW_j\rangle = \delta_{ij}\,dt\,, \qquad (23)$$

where δ_{ij} is the Kronecker delta and symbols $\langle \cdot \rangle$ means averaging.

In cylindrical coordinates the components of Eq. (22) can be expressed in the form:

$$du'_{l,r} = -\frac{u'_{l,r}}{\tau_L(r,z)}dt + \frac{\left(u'_{l,\theta}\right)^2}{r}dt + \left(\frac{2}{\tau_L(r,z)}\right)^{1/2}\sqrt{\frac{2k(r,z)}{3}}\,dW_r\,, \quad (24)$$

$$du'_{l,\theta} = -\frac{u'_{l,\theta}}{\tau_L(r,z)}dt - \frac{\left(u'_{l,r}u'_{l,\theta}\right)}{r}dt + \left(\frac{2}{\tau_L(r,z)}\right)^{1/2}\sqrt{\frac{2k(r,z)}{3}}\,dW_\theta\,, \quad (25)$$

$$du'_{l,z} = -\frac{u'_{l,z}}{\tau_L(r,z)}dt + \left(\frac{2}{\tau_L(r,z)}\right)^{1/2}\sqrt{\frac{2k(r,z)}{3}}\,dW_z\,, \quad (26)$$

where according to Oestele and Zaichik [20] the Lagrangian time scale (τ_L) is a parameter of primary importance, since it represents the asymptotic value of the time scale of the fluid seen by zero inertial particles, a correction in this time scale must be performed for real particles or bubbles [21]. The model given by Eqs. (22) assumes isotropic turbulence. The characteristic time τ_L is computed away from the boundary layer by the following expression:

$$\tau_L(r,z) = 0.14\frac{k(r,z)}{\varepsilon(r,z)} \quad \text{for } y^+ = \frac{(R-r)\,u^*}{\nu_l} > 100d\,. \quad (27)$$

At the boundary layer we have used the expression obtained by direct numerical simulation (DNS) by Kallio and Reeks [22].

To integrate the stochastic differential equation system formed by Eqs. (24)–(26), we define first the column vector $\underline{X} \equiv \text{column}(u'_{l,r}, u'_{l,\theta}, u'_{l,z})$. Then we write the SDE system in the form:

$$d\underline{X} = \underline{a}(\underline{X}(t),t)\,dt + \sum_{j=1}^{3}\underline{b}^{(j)}\,dW^{(j)}(t)\,, \quad (28)$$

where $\underline{a}(\underline{X}(t),t)$ is the drift vector function, and the coefficients $\underline{b}^{(j)}$ are the diffusion coefficients, that on account of Eqs. (24)–(26) and (28) are given by:

$$\underline{a}(\underline{X}(t),t) = \begin{bmatrix} -\frac{X_1}{\tau_L} + \frac{X_2^2}{r} \\ -\frac{X_2}{\tau_L} - \frac{X_1 X_2}{r} \\ -\frac{X_3}{\tau_L} \end{bmatrix}\,, \quad (29)$$

$$\underline{b}^{(1)} = \begin{bmatrix} (2/\tau_L)^{1/2}\,\sqrt{2k/3} \\ 0 \\ 0 \end{bmatrix}, \quad \underline{b}^{(2)} = \begin{bmatrix} 0 \\ (2/\tau_L)^{1/2}\,\sqrt{2k/3} \\ 0 \end{bmatrix},$$

$$\underline{b}^{(3)} = \begin{bmatrix} 0 \\ 0 \\ (2/\tau_L)^{1/2}\,\sqrt{2k/3} \end{bmatrix}. \qquad (30)$$

The stochastic differential equation system (28) can be integrated using the Îto-Taylor expansion methods developed by Kloeden, Platen $et\ al.$ [23–25]. The simplest of such methods is the Euler-Maruyama integration scheme that as we shall show later agrees with the integration method used by Bocksell and Loth when the integration step is much smaller than the Lagrangian turbulent time scale. The k-th component of the Euler scheme is given by [23]:

$$X_k(t_n + \Delta) = X_k(t_n) + a_k(\underline{X}(t_n), t_n)\,\Delta + \sum_{j=1}^{3} b_k^{(j)}(t_n)\,\Delta W^{(j)}\,, \qquad (31)$$

where Δ is the time integration step, and $\Delta W^{(j)}$ is the increment of the j-th Wiener process given by:

$$\Delta W^{(j)} = \int\limits_{t_n}^{t_n+\Delta} dW^{(j)}(s)\,ds = \sqrt{\Delta}\,\xi_j\,, \text{ with } \xi_j \in N(0,1) \qquad (32)$$

being ξ_j a Gaussian random variable with normal sistribution with zero mean and unit variance, the range of n is the number N_s of time steps.

From Eq. (31) and on account of the expressions for the components of the drift and diffusion terms we can write:

$$u'_{l,r}(t_n + \Delta) = u'_{l,r}(t_n) - \frac{u'_{l,r}(t_n)}{\tau_L}\Delta + \frac{\left(u'_{l,\theta}(t_n)\right)^2}{r}\Delta + \left(\frac{2}{\tau_L}\right)^{1/2}\sqrt{\frac{2k}{3}}\,\Delta W_r\,, \qquad (33)$$

$$u'_{l,\theta}(t_n + \Delta) = u'_{l,\theta}(t_n) - \frac{u'_{l,\theta}}{\tau_L}\Delta - \frac{\left(u'_{l,r}u'_{l,\theta}\right)}{r}\Delta + \left(\frac{2}{\tau_L}\right)^{1/2}\sqrt{\frac{2k}{3}}\,\Delta W_\theta\,, \quad (34)$$

$$u'_{l,z}(t_n + \Delta) = u'_{l,z}(t_n) - \frac{u'_{l,z}}{\tau_L}\Delta + \left(\frac{2}{\tau_L}\right)^{1/2}\sqrt{\frac{2k}{3}}\,\Delta W_z\,. \qquad (35)$$

We must notice that the values of the turbulent kinetic energy k and the characteristic Lagrangian time τ_L depend on the position seen by the bubble at time t_n. Also is very easy to check that when in the integration scheme used by Bocksell and Loth [8] to account for the fluid fluctuations, we expand the exponentials $\exp(-\Delta/\tau_L)$ and $\exp(-2\Delta/\tau_L)$ in Taylor series retaining only the first order terms, then we obtain the Euler-Maruyama integration scheme that we have used previously.

In computing the turbulence kinetic energy that appears in Eqs. (22) we must consider the turbulence induced by the bubbles in the liquid phase. We have considered that the turbulence kinetic energy induced by the bubbles depends on the void fraction and the Reynolds number for the bubbles so we write for the total turbulence to be considered in (22):

$$k = k_b + k_l \ , \tag{36}$$

where the turbulence k_b induced by the bubbles is given by the expression:

$$k_b = C_{Ib}\, \alpha \operatorname{Re}_b \ , \tag{37}$$

where α is the vaoid fraction. The value of C_{Ib} is chosen equal to $5.5{\times}10^{-5}$, which provides good results for the experiments performed at a liquid velocity of 2 m/s, as we will display later. However if we assume that this constant depends also on the gradient of the void fraction we may write:

$$C_{Ib} = C_{Ib1} + C_{Ib2}\nabla\alpha \ , \tag{38}$$

where $C_{Ib1}{=}\ 2.0{\times}10^{-5}$, $C_{Ib2}{=}\ 5.5{\times}10^{-4}$, and ∇ denotes the gradient operator. These values provided good results for the experiments performed at 2 and 3 m/s.

To finish this section we must say that when the bubbles move in the axial direction inside the pipe they expand its size because the pressure exerted by the liquid column diminishes. This expansion is computed by the program SAMBUTORY [11] by taking into account the pressure exerted by the water column over the bubble that depends on the vertical distance from the bubble surface to the free surface in the upper tank and of the average void fraction above the bubble $<\alpha>$, and is given by $\rho_l g(1-<\alpha>)(H-z)$. Because the difference of pressures between the gas and the liquid is given by:

$$p_g - p_l = p_g - \left[\rho_l g(1-<\alpha>)(H-z) + p_0\right] = \frac{2\sigma}{R_b} \ , \tag{39}$$

where p_0 is the pressure in the upper part of the column. The bubbles are created in a mixing chamber were we inject air through a porous sinter material as described in detail in Section 3. Each bubble of a given radius, R_b, contains, when it leaves the mixing chamber, a mass of air that we denote by m_0, and that it is conserved. If $p_{g0} = p_g(z = 0)$ denotes the gas pressure inside the bubble at $z = 0$. Then applying the perfect gas law and on account that the gas mass m_0 (mainly air) inside the bubble practically does not change, we may write that the gas pressure at an arbitrary height, z, satisfies the equation:

$$p_g(z)V_b(z) = \frac{m_0}{M_g}R_g\,T \Rightarrow p_g(z) = \frac{m_0}{\frac{4}{3}\pi\,R_b^3(z)}\frac{R_g}{M_g}\,T \;, \qquad (40)$$

where V_b is the bubble volume, M_g is the molecular weight of gas, and R_g is the universal constant of the gas.

Substituting the expression for $p_g(z)$ obtained from the gas law into Eq. (24), there is obtained the following cubic equation in $R_b(z)$:

$$R_b^3(z) + \left\{\frac{2\,\sigma}{\rho_l g(1-<\alpha>)(H-z)+p_0}\right\} R_b^2(z) -$$
$$\frac{3m_0 R_g T}{4\pi\,M_g(\rho_l g(1-<\alpha>)(H-z)+p_0)} = 0 \;, \qquad (41)$$

where H is the distance from the entrance of the pipe, to the free surface of the tank located above the pipe. When Eq. (41) is solved, it is found that it has one real and two imaginary solutions, therefore we can obtain the variation of the bubble radius with the height [11].

2.3 Governing RANS equations for the continuous CFD model in 3D cylindrical geometry

We have coupled the previous Lagrangian and 3D random walk models to an Eulerian model described by the time dependent Reynolds averaged governing equations for the momentum of the liquid continuous phase. In this model no condensation is included and we have assumed that the liquid phase behaves as a Newtonian incompressible fluid with stresses dominated by the turbulence. Two different codes were coupled. The first one was a 2D Eulerian model in (r,z) coordinates and with azimuthal symmetry, whereas the second one was a 3D Eulerian code in (r, θ, z) coordinates. The conservation equations were solved by the finite volume method and the

simpler algorithm in both codes. The equations solved in the 3D case were the following ones:

- radial component of the momentum equation

$$\alpha_l \rho_l \left(\frac{\partial \bar{u}_{l,r}}{\partial t} + \vec{\bar{u}}_l . \vec{\nabla} \bar{u}_r \right) = -\alpha_l \frac{\partial p}{\partial r} + \rho_l \frac{1}{r} \frac{\partial}{\partial r} \left(-\alpha_l \, r \overline{u'^2_{l,r}} \right) +$$
$$+ \rho_l \frac{\partial}{\partial z} \left(-\alpha_l \overline{u'_{l,r} u'_{l,z}} \right) + \rho_l \frac{1}{r} \frac{\partial}{\partial \theta} \left(-\alpha_l \overline{u'_{l,r} u'_{l,\theta}} \right) + f_{i,r} , \qquad (42)$$

- axial component of the momentum equation

$$\alpha_l \rho_l \left(\frac{\partial \bar{u}_{l,z}}{\partial t} + \vec{\bar{u}}_l . \vec{\nabla} \bar{u}_{l,z} \right) = -\alpha_l \frac{\partial p}{\partial z} + \rho_l \frac{1}{r} \frac{\partial}{\partial r} \left(-\alpha_l \, r \, \overline{u'_{l,r} u'_z} \right) +$$
$$+ \rho_l \frac{1}{r} \frac{\partial}{\partial \theta} \left(-\alpha_l \, \overline{u'_{l,r} u'_\theta} \right) + + \rho_l \frac{\partial}{\partial z} \left(-\alpha_l \, \overline{u'^2_{l,z}} \right) - \alpha_l \rho_l g + f_{i,z} , \quad (43)$$

- azimuthal component of the momentum equation

$$\alpha_l \rho_l \left(\frac{\partial \bar{u}_{l,\theta}}{\partial t} + \vec{\bar{u}}_l . \vec{\nabla} \bar{u}_{l,\theta} \right) = -\alpha_l \frac{1}{r} \frac{\partial p}{\partial \theta} + \rho_l \frac{1}{r} \frac{\partial}{\partial r} \left(-\alpha_l \, r \, \overline{u'_{l,r} u'_{l,\theta}} \right) +$$
$$+ \rho_l \frac{1}{r} \frac{\partial}{\partial \theta} \left(-\alpha_l \, \overline{u'^2_{l,\theta}} \right) \rho_l \frac{\partial}{\partial z} \left(-\alpha_l \, \overline{u'_{l,z} u'_{l,\theta}} \right) + f_{i,\theta} , \quad (44)$$

where $f_{i,r}$, $f_{i,\theta}$ and $f_{i,z}$ are the components of the interfacial forces per unit volume in the radial, azimuthal and axial directions respectively, being $\alpha_l = 1 - \alpha$ the fraction of liquid phase and a bar means averaging.

The Reynolds shear and normal stresses in the k-ε model are modeled by the effective viscosity formulation, which is a direct extension of the laminar deformation law:

$$(\tau_{r z})_t = -\rho_l \, \overline{u'_{l,r} u'_{lz}} = \mu_t \left(\frac{\partial \bar{u}_{l,r}}{\partial z} + \frac{\partial \bar{u}_{l,z}}{\partial r} \right) , \qquad (45)$$

$$(\tau_{r \theta})_t = -\rho_l \, \overline{u'_{l,r} u'_{l\vartheta}} = \mu_t \left(\frac{1}{r} \frac{\partial \bar{u}_{l,r}}{\partial \theta} + \frac{\partial \bar{u}_{l,\theta}}{\partial r} \right) , \qquad (46)$$

$$(\tau_{\theta z})_t = -\rho_l \, \overline{u'_{l,\theta} u'_{lz}} = \mu_t \left(\frac{\partial \bar{u}_{l,\theta}}{\partial z} + \frac{1}{r} \frac{\partial \bar{u}_{l,z}}{\partial \theta} \right) , \qquad (47)$$

$$\sigma_r = -\rho_l \, \overline{u'^2_{l,r}} = 2 \, \mu_t \left(\frac{\partial \bar{u}_{l,r}}{\partial r} \right) - \frac{2}{3} \rho_l \, k , \qquad (48)$$

$$\sigma_z = -\rho_l \overline{u_{l,z}'^2} = 2\,\mu_t \left(\frac{\partial \bar{u}_{l,z}}{\partial z}\right) - \frac{2}{3}\rho_l\, k \ , \qquad (49)$$

$$\sigma_\theta = -\rho_l \overline{u_{l,\theta}'^2} = 2\,\mu_t \left(\frac{1}{r}\frac{\partial \bar{u}_{l,\theta}}{\partial \theta}\right) - \frac{2}{3}\rho_l\, k \ , \qquad (50)$$

where the turbulent eddy viscosity is given according to Launder and Spalding [26] by:

$$\mu_{t,l} = c_\mu\,\rho_l\,\frac{k^2}{\varepsilon} \ , \qquad (51)$$

and subscript t referes to turbulent flow.

According to Dhotre, Smith and Niceno [27] the incorporation of the bubble induced viscosity $\mu_{Ib,l}$ to μ_t does not alter the simulation results, so in this model we have not considered this contribution to the effective viscosity. Finally, we have used to calculate the turbulence energy and the dissipation rate the standard k-ε model with the model constants suggested by Launder and Spalding [26].

3   Layout of the experimental facility, instrumentation, measurement techniques, processing of the signals and experiments

Figure 2 displays the outline of the experimental facility used to perform the experimental work. It is a thermohydraulic loop, with a test section, a lower plenum where air bubbles and water are mixed in a chamber that produces bubbly flow or cap/slug flow, and an upper plenum where the air is separated from the liquid. The test section is a round transparent tube made up of plexiglas with constant area, the inner diameter is 52 mm and the length of the section is 3340 mm. We use purified water as working fluid, and the water circulation is provided by two centrifugal pumps controlled by a frequency controller. The air is supplied by an air compressor and it is introduced to the test section through a porous sinter element with an average pore size of 40 μm installed below the mix chamber at the lower plenum. The air and water temperature is kept constant during the test. The conductivity probe measurements were performed at three axial locations, $z/D = 2$, 36 and 56, (where D is the tube diameter), named port INF, MED and SUP, as displayed in Fig. 3, also we display the layout of each port. At each port the pressure is measured by a precision pressure transmitter.
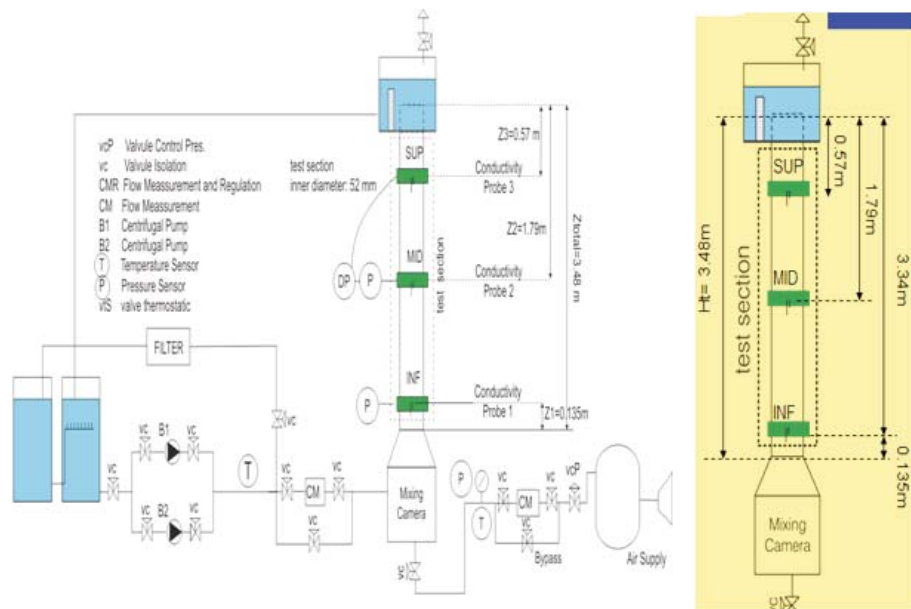
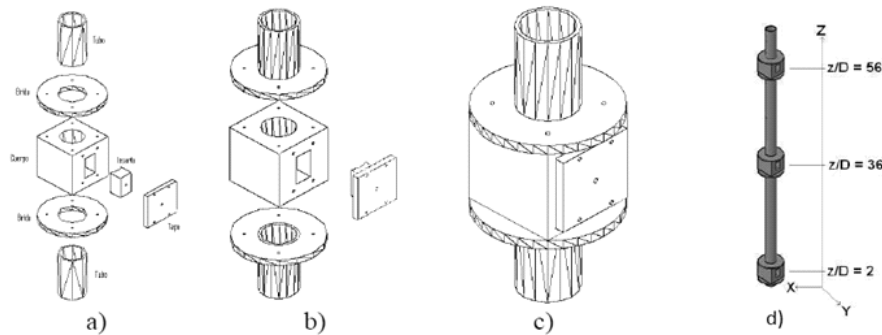Figure 2. PUMA facility layout and detail of the test section.

Figure 3. Design of the ports for the sensor conductivity probe and location of the ports in the test pipe.

3.1 Four-sensors conductivity probe design

The four-sensor probe is basically a phase identifier. The model developed at the Polytechnic University of Valencia (Spain) together with the Jaume I University of Castellón (Spain) consists of four sensors made of stainless

steel, coated with gold, with a diameter of 0.26 mm. The vertical distance between the front tip and the rear sensors was about 1.5 mm. Each sensor is insulated using an insulating varnish except on its tips. Figure 4 displays the schematic design of the probe with the larger tip at one side denoted as FOA, also this figure displays the automatic positioning mechanism of the conductivity probe by means of a stepper driver.
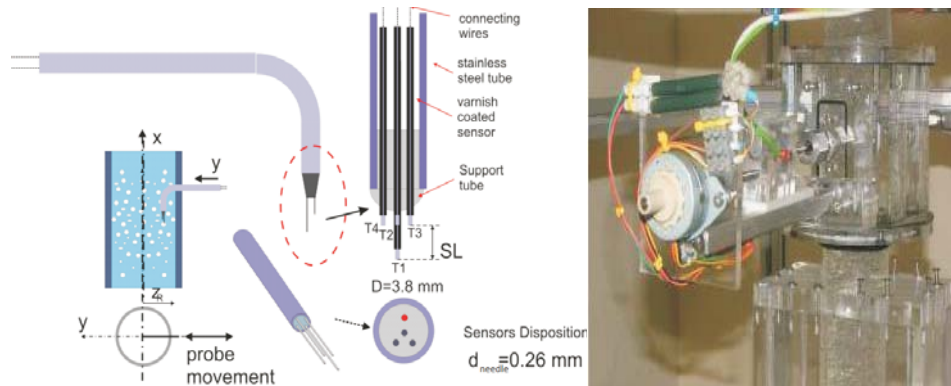
Figure 4. Four-sensors conductivity probe scheme FOA and automatic positioning of the probe by means of a stepper driver.

The sensor geometric configuration of the probes can change from one design to another. For this work we choose the design F0X, with the large tip in the center, and F0A, with the largest tip at one side as displayed in Fig. 4. The largest sensor shown as upper one in cross-sectional view of the probe (Fig. 4 sensor disposition) is called the front sensor or upstream sensor because is the first one that touches the bubble, and the other sensors which are shorter are located in the same plane, are called the rear or downstream sensors. Both geometrical configurations give good and very similar results. The F0X configuration gives better results in positions very close to the wall, with more robust physical sense. The second configuration, F0A, gives the best results when we need to detect large bubbles or when velocity of the liquid is high. More experimental work and a detailed redesign have to be done in order to give more answers about the selection of a suitable design.

The probe was attached to a mechanical traverse mechanism moved by a stepper driver along the radial direction of the test section as displayed in Fig. 4. The *National Instruments* acquisition board of 16 bits was used to acquire the voltage signal of the probe. The sampling frequency was set to 45 kHz for each sensor of the probe, with a sampling time of 45 s.

3.2   Signal processing

The signal processing technique is very important for using the conductivity probe. We can divide this process into two parts; the first one is the conditioning process that consists in filtering, normalizing the signal to convert the signal into a squared one, and finally applying the interface-pairing process. This signal conditioning is very similar to the one proposed by Kim [28]. The second part concerns the processing itself, where the calculation of the physical magnitudes is performed.

The first step is to apply a moving average filtering to the raw signal to eliminate the high frequency noise, mainly produced by the electronic devices. The next step is the generation of squared signals. This step is performed as follows, first we determine the maximum and minimum values of the signal, and the signal values are categorized in six levels. Then, the most probable values for the lowest and highest signal levels are used to normalize the signal. Then, the signal is binarized using a threshold value. This threshold value is very useful to avoid the noise in the measurement. In our experimental facility the best value for the threshold, based on experimental observations, is about 10% of the voltage supply to the probe, and it matches with the value proposed by Kim [28]. Also it is necessary to take into account the slope of the signal near the threshold value to correct the apparent residence time of the i-th bubble denoted by Δt_i as displayed in Fig. 5, with a correction time $\Delta t_{c,i}$ that is the time that the sensor tip is touching the bubble but the signal value (V) is below the threshold, i.e. $V_{water} < V < V_{threshold}$. We have considered an averaged value for this extra time of the bubble residence time.

When the signals are normalized and are converted into squared signals, we initiate the interface-pairing signal process that consists in the determination of the initial time in the front sensor. To begin this process we record the initial time of each squared signal for each sensor. Then, we take these time values from the front sensor, and for each time value we look for the signal produced by the same bubble in the downstream sensors. To achieve this goal, we estimate the interfacial velocity using a very simple drift flux model, and with the distance among the sensors, we estimate the flying time of this bubble from the front to the rear sensors. Then, within a range of 20% of this time we look for initial times in the signals of the rear sensors. If all the rear sensors have signals into this range, then we consider that the bubble signal is pairing, and the bubble signal is considered an effective one. If some of the rear sensor signals are missed, then the bubble
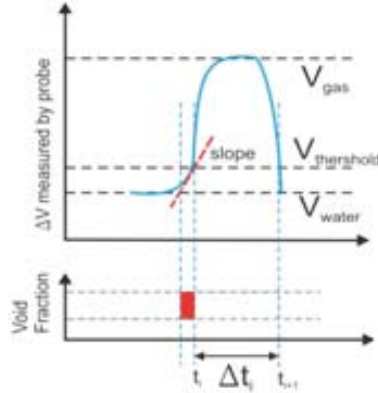
Figure 5. Slope of the signal near the thereshold value.

signal is considered as a missing bubble. When the process is finished, we consider the signals that touch the rear sensors and not the front sensor, which are called non-pairing rear sensors signals. Now, for each rear sensor signal time, we look for its correspondent pair in the other rear sensors, considering the range of time from the time of the sensor to a maximum of the time taken by the bubble to travel from this sensor to the farther one, with a 20% of margin. We consider both directions, the bubble coming to the sensor or the bubble going away to the other sensors. When this pairing process is finished for one of the rear sensor, the process is rerun for the others signals without considering the signals pairing. At the end, we get the bubble effective signals, and all the missing bubble signals.

The second part concerns the processing itself, where the calculation of the magnitudes is performed.

3.3   Classification of the bubbles in groups

The chord length for each bubble obtained from the signal of the front sensor is used to classify the bubbles in three groups: spherical, distorted and cap/slug. The limits of the groups are obtained from the following formulas [29]:

1. The upper limit of spherical bubbles is given by:

$$D_{spherical} = 4\sqrt{\frac{2\,\sigma}{g\,\Delta\rho}}\, N_{\mu_f}^{1/3} \ \text{ with } \ N_\mu = \frac{\mu_f}{\left(\rho_f\sigma\sqrt{\frac{\sigma}{g\,\Delta\rho}}\right)^{1/2}} \qquad (52)$$

with N_μ being the viscosity number, $\Delta\rho$ is the difference between the liquid and gas densities and μ_f is the liquid viscosity.

2. Upper limit of distorted bubbles

$$D_{distorted} = 4 \sqrt{\frac{\sigma}{g \, \Delta\rho}} \; . \tag{53}$$

3. Upper limit of cap bubbles

$$D_{cap-\max} = 40 \sqrt{\frac{\sigma}{g \, \Delta\rho}} \; . \tag{54}$$

For practical effects the bubbles are classified in two groups: group **1** or spherical/distorted bubbles, and group **2** or cap/slug bubbles.

3.4 Determination of the local void fraction and the interfacial area concentration

The void fraction is obtained from summation over all the residence times of the bubbles touching the front probe, by means of the expression:

$$\alpha = \frac{\sum_{i=1}^{N_b} (\Delta t_i + \Delta t_{c,i})}{T_{sample}} \; , \tag{55}$$

where Δt_i is the apparent residence time, and $\Delta t_{c,i}$ is the correction to the apparent residence time as explained previously; T_{sample}, is the total sampling time, and N_b is the number of bubbles recorded by the sensor during the sampling time. The interfacial area concentration is obtained from the expression [30–32]:

$$\bar{a}_I(\vec{r}) = \frac{1}{T_{sample}} \sum_{j=1}^{N_{int}} \frac{1}{|\vec{u}_{I,j} \cdot \vec{n}_{I,j}|} \; , \tag{56}$$

where N_{int} is the number of interfaces crossing the point $\vec{r}$ during the time T_{sample}, $\vec{u}_{I,j}$ is the interfacial velocity of the j-th interface crossing the point $\vec{r}$, and $\vec{n}_{I,j}$ is the unit vector normal to the j-th interface at point $\vec{r}$.

With the four sensor conductivity probe we can measure the interfacial area concentration as follows [31]:
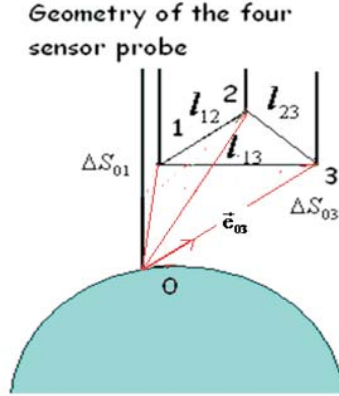
Figure 6. Geometry of the four sensor conductivity probe, (0) is the front sensor and (1), (2), and (3) the rear sensors.

1. First from the geometry of the four sensor conductivity probe, we can obtain the unit vectors $\vec{e}_{0k}$ in the directions from the front tip (0) to the rear tips (1), (2) and (3). The components of these unit vectors are according to Fig. 6:

$$\vec{e}_{ok} = \frac{\vec{r}_k - \vec{r}_0}{\Delta S_{0k}} = \left(\cos\eta_{x0k}, \cos\eta_{y0k}, \cos\eta_{z0k}\right), \quad k = 0, 1, 2, 3 \quad (57)$$

2. The measured velocities $\vec{u}_{m,0k}$ in the directions of the previous unit vectors are given by the following expressions:

$$\vec{u}_{m,0k} = \frac{\Delta S_{0k}}{\Delta t_{0k}}\, \vec{e}_{0k} \quad (58)$$

being ΔS_{0k} the distance between the front sensor and the k-th rear sensor and Δt_{0k} the time needed by the interface to travel from the front sensor to the k-th rear sensor.

3. Then we use the interfacial measure theorem [29,30], that gives us the projection of the interfacial velocity on the normal to the bubble surface in terms of the known measured velocities $\vec{u}_{m,0k}$ and that can be expressed in the form:

$$\vec{n}_{I,j} \cdot \vec{u}_{m,0k} = \vec{n}_{I,j} \cdot \vec{u}_{I,j} = u_{n,j}\,. \quad (59)$$

This theorem can be expressed on account of Eq. (58) as follows:

$$\vec{n}_{I,j} \cdot \vec{u}_{m,0k} = \vec{n}_{I,j} \cdot \vec{e}_{0k} \, u_{m,0k} = u_{n,j} \ . \tag{60}$$

The previous equation is equivalent to the following system of four equations with four unknowns:

$$\begin{bmatrix} \cos\eta_{x01} & \cos\eta_{y01} & \cos\eta_{z01} \\ \cos\eta_{x02} & \cos\eta_{y02} & \cos\eta_{z02} \\ \cos\eta_{x03} & \cos\eta_{y03} & \cos\eta_{z03} \end{bmatrix} \begin{bmatrix} \cos\eta_x \\ \cos\eta_y \\ \cos\eta_z \end{bmatrix}_j = \begin{bmatrix} u_{n,j}/u_{m,01} \\ u_{n,j}/u_{m,02} \\ u_{n,j}/u_{m,03} \end{bmatrix} \ , \tag{61}$$

$$\cos^2\eta_x + \cos^2\eta_y + \cos^2\eta_z = 1 \ ,$$

where the rows of the matrix are the components of the unit vectors $\vec{e}_{0k}$ and $(\cos\eta_x, \cos\eta_y, \cos\eta_z)$ are the components of the unit vector $\vec{n}_{I,j}$, normal to the j-th interface. The system of equations (38) can be solved easily by the Kramer's rule to obtain the components of $\vec{n}_{I,j}$ in terms of $u_{n,j}$ then using the fact that $\vec{n}_{I,j}$ is a unit vector we obtain $u_{n,j}$, that is given by:

$$u_{n,j} = \frac{A_0}{\sqrt{A_{1,j}^2 + A_{2,j}^2 + A_{3,j}^2}} \ , \tag{62}$$

where we have defined the following determinants:

$$A_0 = \begin{vmatrix} \cos\eta_{x01} & \cos\eta_{y01} & \cos\eta_{z01} \\ \cos\eta_{x02} & \cos\eta_{y02} & \cos\eta_{z02} \\ \cos\eta_{x03} & \cos\eta_{y03} & \cos\eta_{z03} \end{vmatrix} \ , \quad A_{1,j} = \begin{vmatrix} \left(\frac{1}{u_{m,01}}\right)_j & \cos\eta_{y01} & \cos\eta_{z01} \\ \left(\frac{1}{u_{m,02}}\right)_j & \cos\eta_{y02} & \cos\eta_{z02} \\ \left(\frac{1}{u_{m,03}}\right)_j & \cos\eta_{y03} & \cos\eta_{z03} \end{vmatrix}$$

$$\tag{63}$$

$$A_2 = \begin{vmatrix} \cos\eta_{x01} & \left(\frac{1}{u_{m,01}}\right)_j & \cos\eta_{z01} \\ \cos\eta_{x02} & \left(\frac{1}{u_{m,02}}\right)_j & \cos\eta_{z02} \\ \cos\eta_{x03} & \left(\frac{1}{u_{m,03}}\right)_j & \cos\eta_{z03} \end{vmatrix} \ , \quad A_3 = \begin{vmatrix} \cos\eta_{x01} & \cos\eta_{y01} & \left(\frac{1}{u_{m,01}}\right)_j \\ \cos\eta_{x02} & \cos\eta_{y02} & \left(\frac{1}{u_{m,02}}\right)_j \\ \cos\eta_{x03} & \cos\eta_{y03} & \left(\frac{1}{u_{m,03}}\right)_j \end{vmatrix} \ .$$

$$\tag{64}$$

Once we have obtained the projections of the velocities on the normal i.e. $u_{n,j}$, then we can obtain the interfacial area concentration using Eq. (35).

3.5 Experiments

The flow conditions have been chosen measuring the superficial liquid and air velocities and the average void fraction at position $z/D = 56$ for each run

condition. All the run conditions (Tab. 1) are in the bubbly flow regime, and only for the highest void fractions appear some large cups, near the transition from bubbly to cap/slug regime. For each liquid velocity conditions we have performed the experiments with at least five gas conditions ranging from 5 to up 25%, except in the case when the superficial liquid velocity $j_f = 0.5$ m/s where an extra case was tested near the transition from bubbly to cap/slug regime. At the setup of each run the void fraction was also measured by a pressure sensor at $z/D = 56$. Details about the experiments and the facility can be found in Mendez thesis [29].

To check the methodology used in the measurements, the experiments F01G01 and F01G02 were also performed with boundary conditions close to that of the experiments performed by Hibiki, Ishii and Xiao [34]. The distributions of void fraction and interfacial area concentration measured in our experiments were compared with the distributions obtained by Hibiki, Ishii and Xiao [33], the results in general agree pretty well as displayed in Fig. 7.

We also performed the measurements with two types of conductivity probes as we mentioned earlier in section 3.1: with the large tip in the center denoted as FOX, and with the large tip in one side denoted FOA. In Fig. 8 we display the void fraction and the interfacial area concentration (IAC), versus the relative radial distance to the center of the pipe r/R, where R is the tube radius for the case F03 with $j_f = 2$ m/s, at the upper port with $z/D = 56$. We observe in this experiment that when the void fraction is small the void fraction distribution have the typical peak distribution near the wall, known as wall-peak. This distribution is produced by the small bubbles that tend to migrate to the wall due to the lift force. The height of the peak is mainly determined by the balance between the lift force on the bubbles that push them toward the wall and the wall lubrication and deformation forces that have the opposite direction. Also is very important in this balance the motion of the bubbles due to the turbulent diffusion that tends to diminish the height of the peak. We also notice in Fig. 8 that when the void fraction increases to values of the order of 0.25, then the void fraction distribution becomes a core peak distribution. This is due to the presence of a bigger number of larger bubbles (cap/slug) due to the increase of the void fraction; also we have more bubbles coalescence and this phenomenon also increases the size of the bubbles. The lift force when acting on larger bubbles pushes them toward the center and in this way this produces a core peak.
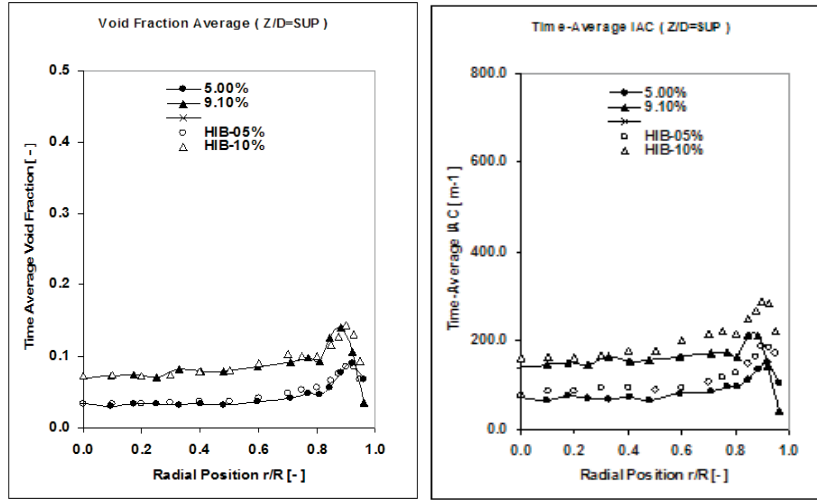
Figure 7. Comparison of experiments performed by Hibiki, Ishi and Xiao for the void fraction and the interfacial area concentration [25], with the experimental results of Chiva *et al.* [26], for the conditions of experiments F01G01 and F01G02, displayed in Tab. 1.

Table 1. Experimental flow conditions for test F.

|	j_f =0.5 [m/s]			j_f =1.0 [m/s]	
Run	j_g [m/s]	$< \alpha >$ [%]	Run	j_g [m/s]	$< \alpha >$ [%]
F01G00	0.00	0.00	F02G00	0.00	0.00
F01G01	0.075	5.14	F02G01	0.121	4.84
F01G02	0.075	10.38	F02G02	0.135	9.36
F01G03	0.077	15.73	F02G03	0.144	14.97
F01G04	0.081	21.10	F02G04	0.173	22.35
F01G05	0.122	25.86	F02G05	0.232	29.88
F01G06	0.144	26.87			
	j_f =2.0 [m/s]			j_f =3.0 [m/s]	
	j_g [m/s]	$< \alpha >$ [%]		j_g [m/s]	$< \alpha >$ [%]
F03G00	0	0.00	F04G00	0.00	0.00
F03G01	0.209	3.69	F04G01	0.363	5.04
F03G02	0.231	8.18	F04G02	0.407	9.76
F03G03	0.268	14.90	F04G03	0.444	14.7
F03G04	0.280	20.1	F04G04	0.499	19.5
F03G05	0.336	26.2	F04G05	0.571	24.3
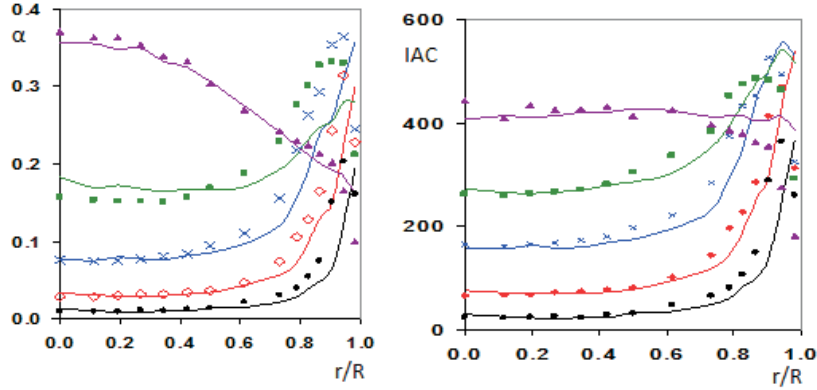
Figure 8. Void fraction versus r/R and IAC versus r/R for case FO3 with $j_f = 2$ m/s, at the upper port $z/D = 56$. Solid symbol correspond to F0A probe configuration, and without symbol (continuous line) to F0X probe. Black (●) G01, Red (◇) G02, (X) G03, Green (■) G04, Violet (▲) G05.

4   Experiments performed changing the surface tension

A set of experiments denoted with the letters C, D, E were performed adding small amounts of 1-butanol and with the same boundary conditions than experiment B (no 1-butanol added). These amounts were 9, 39, and 75 ppm for experiments C, D, and E respectively. The goal of these experiments was to study the effect of changing the surface tension on the two phase flow local parameters. The effect of adding small amounts of 1-butanol is to reduce the surface tension of the liquid phase. Obviously this affects the size of the bubbles by reducing their size. For each one of the experimental series the liquid superficial velocities were 0.5, 1 and 2 m/s. In addition, for each liquid superficial velocity, the gas superficial velocity was varied to have void fraction values close to 5, 10, 15 and 20%. Table 2 displays the flow conditions for the set of experiments B. Similar conditions were used for tests C, D and E.

Now we display the results of the tests B and D in the same figures, in order to see the effect of the changes in the surface tension on the void fraction distribution. Test D was performed with a 1-butanol concentration of 39 ppm and the measured surface tension was reduced from 72.2 ± 0.8 in ordinary water to 65.7 ± 0.9 when adding the 1-butanol. These kind of experimental studies are very interesting because when increasing the

temperature the surface tension diminishes and in this way we can know what it is expected to happen at higher temperatures.

Table 2. Experimental flow conditions for test B.

| j_l= 0.498 [m/s]			j_l= 0.994 [m/s]			j_l= 1.994 [m/s]		
Run	j_g[m/s]	$\langle\alpha\rangle_{z/d=upper}$	Run	j_g[m/s]	$\langle\alpha\rangle_{z/d=upper}$	Run	j_g[m/s]	$\langle\alpha\rangle_{z/d=upper}$
B01G00	0.000	0.00	B02G00	0.000	0.00	B03G00	0.00	0.00
B01G01	0.035	5.37	B02G01	0.075	6.77	B03G01	0.134	5.27
B01G02	0.080	10.47	B02G02	0.166	12.09	B03G02	0.347	8.20
B01G03	0.129	15.70	B02G03	0.271	16.35	B03G03	0.635	17.07
B01G04	0.188	20.18	B02G04	0.377	19.31	B03G04	1.270	21.77
B01G05	0.266	21.57	B02G05	0.492	21.10	B03G05	2.390	24.43
B01G06	0.503	30.36	B02G06	0.621	23.81	B03G06	–	–
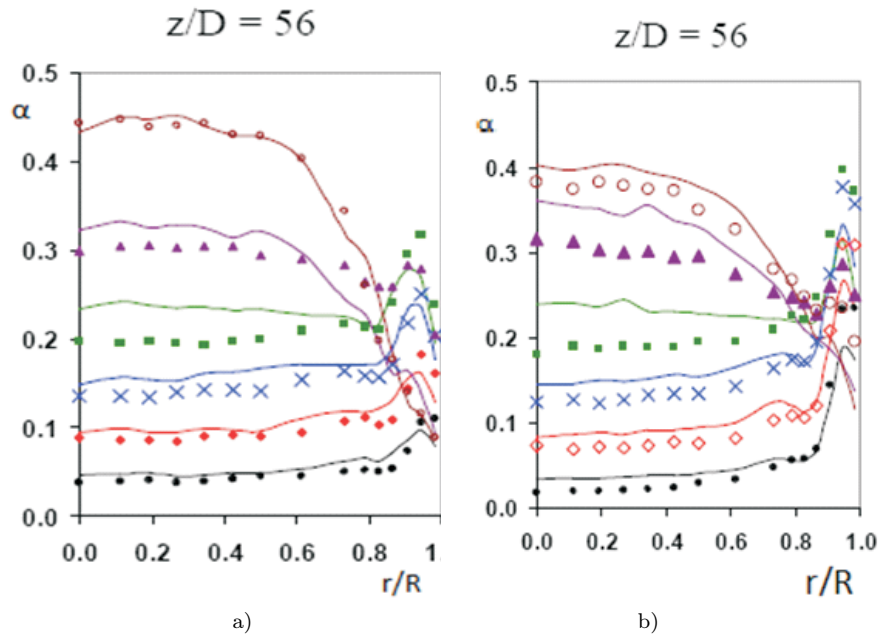
Figure 9. Test results for different gas superficial velocities at $z/D = 56$: a) for runs D01 and B01; b) for runs D02 and B02.

Figure 9 deserves several comments. The first one is that when we add small amounts of 1-butanol the size of the bubbles diminishes and we have more bubbles of small size that tend to migrate toward the wall, increasing

the height of the wall peak. This effect is clearly observed in runs D01G01, D01G02, D01G03 and D01G04, when comparing these runs with the runs B01G01, B01G02, B01G03, and B01G04, performed with pure water, we notice that the height of the wall peak increases when we add 1-butanol. The same effect is also observed in runs D02G01, D02G02, D02G03 and D02G04.

But there is also another effect that is clearly displayed in Figs. 9a and 9b, and is that the transition conditions from wall peak to core peak flow changes when we reduce the surface tension maintaining the same liquid and gas superficial velocities. For instance in run B01G05 we have core peak flow, while in run D01G05 we have wall peak flow, as is observed in Fig. 9a for the same boundary conditions of the gas and liquid phases. When adding a small amount of 1-butanol we have a small peak near the wall for case D01G05 and the void fraction distribution in the central region of the tube becomes flatter. This effect shows clearly that diminishing the surface tension changes the boundaries of the flow map. This same effect it is also observed in runs B02G05 and D02G06. B02G05 is core peak while D02G05 is wall peak, and the void fraction distribution for run D02G05 becomes flatter at the central region and displays a peak near the wall.

5   Computational results and comparison with experiments

The Lagrangian and the 3D random walk models were programmed in a code denoted SAMBUTORY (sampling bubble's trajectories) that was coupled to a 2D Eulerian solver in (r,z) coordinates and to a 3D solver.

The dispersed phase is computed by tracking the bubbles along its trajectories on account of the forces acting on them as explained in Section 2. The bubbles are generated with a uniform distribution at the bottom of the pipe, and the diameter of the bubbles is sampled uniformly in the interval [2.1 mm, 2.9 mm] according to the experimental data for the Sauter mean diameter. Then each individual bubble is tracked until it reaches the z coordinate of 3 m. At this position the radial coordinate of each individual bubble, its volume, and its interfacial area are stored in a counter to compute the radial distribution for the void fraction and the interfacial area concentration. When each individual bubble is moving in 3D along its trajectory its position changes and as a consequence the fluid velocity field that it is being seen by this bubble and is computed by the Eulerian

solver also changes. The total number of bubbles tracked to compute the void fraction distribution is 8000.

The turbulence field that is felt by the bubbles has two components, one is the turbulence generated by the liquid and the other one is the turbulence induced by the bubbles. Since the fluctuating component of the liquid velocity field that is seen by the bubbles depends on the total turbulent energy $k(r,z)$ at each position (r,z), in the 2D solver and to compute the turbulence induced by the bubbles we need the void fraction distribution, that is not known a priori. Then we must perform several iterations to obtain a good void fraction distribution that allows an evaluation of the turbulence induced by the bubbles at each radial position. These iterations are performed in a self-consistent manner as follows: we start with the liquid turbulence alone in the continuous random walk model, then solving the RANS equations for the continuous phase and the Lagrangian model for the bubbles we obtain the first iterated value for the void fraction distribution that is more peaked than the experimental one because it does not take into account the random walk diffusion induced by the bubbles themselves. This distribution is used as an input to integrate the Lagrangian equations again and in this way we obtain a second iterated value of the void fraction distribution, after three or four iterations the void fraction distribution converges and gives values that are close to the experimental ones as displayed in Fig. 10 for the cases with $j_f = 2$ m/s. In this case the turbulence induced by the bubbles was computed with Eq. (23) using a constant value for $C_{Ib} = C_{Ib0} = 5.5 \times 10^{-5}$, and the calculated points are represented by triangles, while the experimental points are denoted by solid circles. Finally the empty circles denote the void fraction distribution computed using Eq. (38) for the turbulence induced by the bubbles with $C_{Ib1} = 2.0 \times 10^{-5}$ and $C_{Ib2} = 5.5 \times 10^{-4}$.

The predictions of the void fraction distribution are very good in all the points, also the maximum position of the void fraction distribution and its value is well predicted by the Eulerian-Lagrangian model developed in this paper. The calculations were performed with a 3D solver coupled to the SAMBUTORY code, the results are displayed in Fig. 11, for the same case F03G01. In this figure the crosses (x), denote the (r,z) axissymmetric calculations, while the empty circles denote the 3D calculations with the Eulerian solver. The results improve as displayed in Fig. (11) when we use the 3D Eulerian solver instead of the 2D with (r,z) coordinates and azimuthal symmetry.
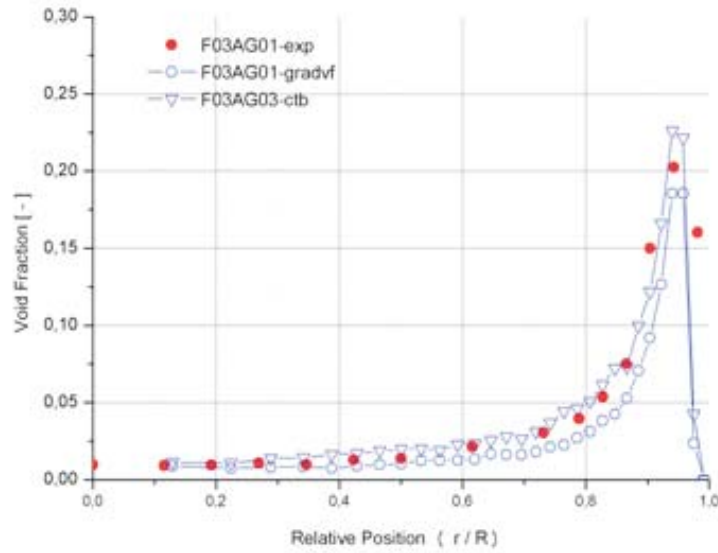
Figure 10. Void fraction profile for run F03G01, $j_f = 2$ m/s, $j_g = 0.209$ m/s. The solid circles denote the experimental results, while the open circles are the calculated ones with $C_{Ib} = C_{Ib1} + C_{Ib2}\nabla\alpha$, and the triangles the calculated with $C_{Ib} = C_{Ib0}$.
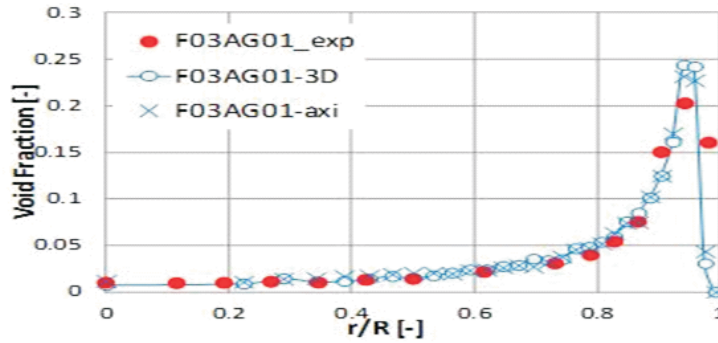

Figure 11. Void fraction profile for run F03G01, $j_f = 2$ m/s, $j_g = 0.209$ m/s. The solid circles denote the experimental results, the open circles are the calculated ones with the 3D Eulerian code and the crosses (x) denote the calculated with the 2D Eulerian solver. Both calculation were performed with $C_{Ib} = C_{Ib0}$.

In Fig. 12 we display the predicted values for the IAC (solid circles) and the experimental values (empty circles and continuous line), computed using Eq. (23) for the turbulence induced by the bubbles. Finally we display in Fig. 13 the results for the interfacial velocity distribution for run F03G01, calculated with the 2D and 3D solvers. Prediction has been made for another cases with $j_f = 1$ m/s and 3 m/s also with very good results.
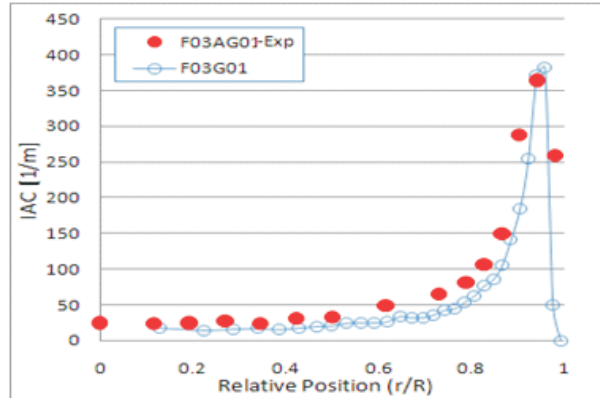

Figure 12. Experimental (solid circles) and computed (open circles) interfacial area concentration for run F03G01.
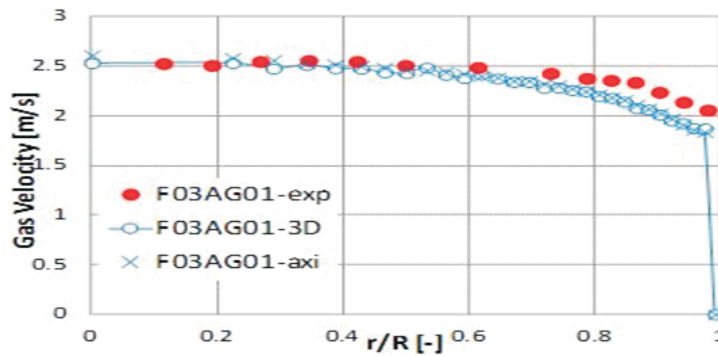

Figure 13. Interfacial area velocity profile for run F03G01. The solid circles denote the experimental results. The open circles are the calculated results with the 3D Eulerian solver and the crosses (x) the calculated values with the 2D (r,z) solver.

6   Conclusions

In this paper we have shown the results of a set of experiments performed with different superficial velocities of gas and liquid phases, covering the transition region from bubbly flow to cap/slug flow. In these experiments the void fraction and the interfacial area concentration were measured at fifteen radial positions and three axial locations. It was shown in these experiments that if for a given superficial velocity of the liquid as for instance $j_l = 2$ m/s, we increase the superficial velocity of the gas phase, then it happens that for gas superficial velocities with void fractions above 20%, a flow regime transition is produced from the wall peak to the core peak as it is shown in Fig. 8. This transition is caused by the appearance of cap and slug bubbles of big size that tends to move toward the pipe center. The causative mechanism of this transition is that the lift force changes it sign for bubbles bigger that around 5.8 mm, that correspond to the Eötwos number around 10.

Then this paper shows the results for a set of experiments performed by adding small amounts of 1-butanol to reduce the surface tension of the water. We have seen that the bubble's size diminish for bubbly flow conditions and we have more small size bubbles that tend to move toward the wall due to the lift force, producing in this way a wall peak higher that the peak produced in the experiments with the same boundary conditions for the liquid and gas phases but without adding 1-butanol.

A phenomenon that has been observed in the experiments by adding 1-butanol is that there is a change in the flow map. When the surface tension is reduced, the transition from the wall peak to the core peak takes place with higher superficial velocities of the gas, for instance as displayed in Fig. 9, the case B02G05 features the core peak that means that the flow regime transition have been already produced, while the case D02G05 with the same boundary conditions but adding a small amount of 1-butanol is exhibiting the wall peak.

In this paper we have developed a model that consists in a Lagrangian model to track the bubble trajectories coupled to a Eulerian model for the continuous phase and a 3D random walk model to take into account the velocity fluctuations that are seen by the bubbles due to the liquid turbulence. The turbulence induced by the bubbles plays an important role in the continuous random walk model because when this mechanism for turbulence production is not included, then the peak for the void fraction profile is higher than the experimental one; in this way we can say that the turbulence

induced by the bubbles increases the bubble turbulence diffusion. Since the void fraction distribution is not known a priori then a self-consistent calculation is performed in order to obtain the void fraction distribution. This is achieved by executing a set of iterations to obtain the true void fraction profile. The first void fraction distribution is obtained by considering only the liquid turbulence. The output of this calculation is a first iterated void fraction distribution that is used as input for the second calculation and so on. The convergence is achieved in three or four iterations.

Another important issue is to notice is that the turbulence induced by the bubbles given by Eq. (23), returns better predictions when we assume that the constant C_{Ib} that appears in Eq. (23) is assumed to depend on the gradient of the void fraction profile as in Eq. (38). Good predictions of the void fraction distributions are obtained for the cases with liquid superficial velocities of 2 and 3 m/s, and also for the interfacial velocity distributions and interfacial area concentrations. Also the Lagrangian and 3D random walk models have been coupled to a 3D Eulerian solver, and it is observed that the results improve when using this last alternative although the computational effort is bigger when this last option is chosen.

Presented here model does not include the coalescence of the bubbles or the break up of the bubbles by interactions with turbulent eddies. Therefore the next step is to include that into Eulerian-Lagrangian, that is the model break-up and coalescence mechanisms in order to go to the cap/slug regime, in this way we could make predictions of the void fraction distribution for several group of bubbles. The model is being improved by including these interaction mechanisms in a full Lagrangian-Eulerian model were group of bubbles are simultaneously tracked, and when the distance between two bubbles is smaller than a certain distance on which the interaction takes place.

References

[1] KLEINSTREUER C. ED: *Two Phase Flow: Theory and Applications.* Taylor and

Francis, New York 1993.

[2] Zaruba A., Lucas D., Prasser H.M., Höhne T.: *Bubble-wall interaction in a vertical gas-liquid flow: Bouncing, sliding and bubble deformations.* Chem. Eng. Sci. **62**(2007), 1591–1605.

[3] Zun I., Kljenak I., Moze S.: *Space-time evolution of the non-homogeneous bubble distribution in upward flow.* Int. J. Multiphase Flow **19**(1993), 1, 151–172.

[4] Prasser H.M., Krepper E., Lucas D.: *Evolution of the two phase flow in a vertical tube, decomposition of gas fraction profiles according to bubble size classes using wire-mesh sensors.* Int. J. Thermal Sci. **41**(2002), 17–28,.

[5] Tomiyama A., Zun I., Higaki H., Makino Y., Sakaguchi T.: *A three-dimensional particle tracking method for bubbly flow simulation.* Nucl. Eng. Des. **175**(1997), 77–86.

[6] Lucas D., Krepper E., Prasser H.M.: *Development of co-current air-water flow in a vertical pipe.* Int. J. Multiphase Flow **31**(2005), 1304–1328.

[7] Krepper E., Lucas D., Prasser, H.M.: *On the modelling of bubbly flow in vertical pipes.* Nucl. Eng. Des. **235**(2005), 597–611.

[8] Bocksell T.L., Loth E.: *Stochastic modelling of particle diffusion in a turbulent boundary layer.* Int. J. Multiphase Flow **32**(2006), 1234–1253.

[9] Dehbi A.: *Turbulent particle dispersion in arbitrary wall-bounded geometries: A coupled CFD-Langevin-equation based approach.* Int. J. Multiphase Flow **34**(2008), 819–828.

[10] Haworth D.C., Pope S.B.: *Generalized Langevin model for turbulent flows.* Physics Fluids **29**(1986), 2, 387–405.

[11] Muñoz-Cobo J.L., Chiva S., Abdelazziz M., Méndez S.: *Coupled Lagrangian and Eulerian simulation of bubbly flows in vertical pipes, validation with experimental data using multisensory conductivity probes and laser Doppler anemometry.* Nucl. Eng. Des. **242**(2012), 285–299.

[12] Tomiyama A.: *Struggle with computational Dynamics.* In: Proc. Third Int. Conf. Multiphase Flow. ICMF-98, Lyon, France, 1998.

[13] Auton T.R.: *The Lift Force on a Spherical Body in a Rotational Flow.* J. Fluid Mech., 183, 199–218, (1987).

[14] Tomiyama A., Tamai H., Zun I., Hosokawa S.: *Transverse migration of single bubbles in simple shear flows.* Chem. Eng. Sci. **57**(2002), 1849–1858.

[15] Antal S.P., Lahey R.T. Jr., and Flaherty, J.E.: *Analysis of two phase flow distribution in fully developped daminar bubbly two-phase flow,* Int. J. Multiphase Flow **17**(1991), 635–652.

[16] Pope S.B.: *Stochastic Lagrangian models of velocitiy in homogeneous turbulent shear flow.* Phys. Fluids **14**(2002), 5, 1696–1702.

[17] Haworth D.C., Pope S.B.: *A generalized Langevin model for turbulent flow.* Phys. Fluids **29**(1986), 2, 387–405.

[18] Veenman, M.P.B.: *Statistical Analysis of Turbulent Flow".* PhD thesis, University of Eindhoven, Eindhoven 2004.

[19] DEHBI A.: *Turbulent particle dispersion in arbitrary wall-bounded geometries: a coupled CFD-Langevin-equation based approach.* Int. J. Multiphase Flow **34**(2008), 819–828.

[20] OESTERLÉ B., ZAICHIK L.I.: *On Lagrangian time scales and particle dispersion modeling in equilibrium shear flows.* Phys. Fluids **16**(2004), 9, 3374–3384.

[21] KALLIO G.A., REEKS M.W.: *A numerical simulation of particle deposition in turbulent boundary layers.* Int. J. Multiphase Flow **3**(1989), 433–446.

[22] POZORSKI J., MINIER J.P.: *On the Lagrangian turbulent dispersion models based on the Langevin equation.* Int. J. Multiphase Flow **24**(1998), 913–945.

[23] KLOEDEN P.E., PLATEN E. EDS.: *Numerical Solution of Stochastic Differential Equations.* Springer Verlag, Berlin 1995.

[24] KLOEDEN P.E., PLATEN, E., SCHURZ, H. EDS.: *Numerical Solution of Stochastic Differential Equations Through Computer Experiments.* Springer Verlag, Berlin 1994.

[25] MUÑOZ-COBO J.L., MONTESINOS M.E., PEÑA J., ESCRIVÁ A., GONZÁLEZ G., MELARA J.: *Validation of reactor noise linear stability methods by means of advanced stochastic differential equations models.* Ann. Nucl. Energy **38**(2011), 1473–1488.

[26] LAUNDER B.E., SPALDING B.: *Mathematical Models of Turbulence.* Academic Press, New York 1972.

[27] DHOTRE M.T., SMITH B.L., NICENO B: *CFD simulation of bubbly flows: Random dispersion model.* Chem. Eng. Sci. **62**(2007), 7140–7150.

[28] KIM S.; FU Y.; ISHII M.: *Study on interfacial structures in slug flows using a miniaturized four-sensor conductivity probe.* Nucl. Eng. Des. **204**(2001), 45–55.

[29] MENDEZ-DIAZ S.: *Experimental Measurement of the Interfacial Area Concentration.* PhD thesis, Universidad Politécnica de Valencia, Valencia 2008 (in Spain).

[30] SHEN X.Y., SAITO K., NAKAMURA M.H.: *Methodological improvement of an intrusive four-sensor probe for the multi-dimensional two-phase flow measurement.* Int. J. Multiphase Flow **31**(2005), 593–617.

[31] DELHAYE J.P., BRICARD P.: *Interfacial area in bubbly flow: experimental data and correlations.* J. Nucl. Eng. Des. **151**(1994), 65–77.

[32] ISHII M.: *Thermo-Fluid Dynamic Theory of Two-Phase Fflow.* Eyrolles, Paris 1975.

[33]] HIBIKI T., ISHI M., XIAO Z.: *Axial interfacial area transport of vertical bubbly flows.* Int. J. Heat Mass Transfer **44**(2001), 1869–1888.

[34] FERZIGER J.H., PERIC M.: *Computational methods for fluid dynamics*, Springer, ISBN 3-540-42074-6, 2002.